PAPER

Check for updates

Redox mediator-modified self-assembled monolayer stabilizes a buried interface in efficient inverted perovskite solar cells†

Shujie Qu,[a] Fu Yang,[a] Hao Huang,*[a] Yiyi Li,[b] Changxu Sun,[a] Qiang Zhang,[a] Shuxian Du,[a] Luyao Yan,[a] Zhineng Lan,[a] Zhiwei Wang,[a] Tongtong Jiang,[a] Peng Cui,[a] Xicheng Ai [ID][b] and Meicheng Li [ID]*[a]

Utilizing a self-assembled monolayer (SAM) of [4-(3,6-dimethyl-9H-carbazol-9-yl)butyl]phosphonic acid as the interfacial layer on NiO_x (Me-4PACz) has been proven to be a feasible approach to improve the photovoltaic performance of inverted perovskite solar cells (PSCs). However, considering the chemical reactivity of the NiO_x surface and inhomogeneous SAM, interface stability is still an urgent issue that needs to be addressed. Herein, methylene blue, a redox molecule, was co-absorbed with Me-4PACz to serve as a functionalized interfacial layer, which effectively enhanced interface stability. Methylene blue could serve as a redox mediator to selectively reduce the high-valence state of Ni species and oxidize metallic Pb^0, suppressing the undesirable interfacial reaction and reducing interfacial defects. Besides, methylene blue could mitigate the uneven dispersion of Me-4PACz through $\pi-\pi$ interaction, which reduced the generation of voids and aggregates, providing a flattened and compact interfacial layer. These effects enabled inverted 0.08 cm^2-PSCs and 1 cm^2-PSCs to achieve efficiencies of 26.39% and 24.89%, respectively. Encouragingly, the device possessed enhanced stability even under harsh damp-heat conditions, retaining 91% of its initial efficiency after 1500 hours of UV irradiation and 90% of its initial efficiency after 1500 hours of operation under 1-sun illumination.

Broader context

Inverted perovskite solar cells (PSCs) have garnered significant attention owing to their remarkable compatibility in tandem solar cells. As an inorganic p-type semiconductor, NiO_x is commonly employed as a hole transport material for advancing inverted PSCs towards commercialization owing to its scalability and cost-effectiveness. However, the presence of surface defects and undesirable interface chemical reactivity hinder the enhancement of device stability. In this work, methylene blue (MB) was co-absorbed with [4-(3,6-dimethyl-9H-carbazol-9-yl)butyl]phosphonic acid (Me-4PACz) as a functionalized interfacial layer. We revealed that MB can mitigate the uneven dispersion of Me-4PACz on the surface of NiO_x, which reduces the generation of voids and aggregates, providing a flattened and compact interfacial layer. Moreover, MB can serve as a redox mediator to selectively reduce the high-valence state Ni species and oxidize metallic Pb^0 while synergistically passivating interfacial defects by constructing a bridge-link structure, which stabilizes the buried interface. As a consequence, inverted 0.08 cm^2-PSCs and 1 cm^2-PSCs achieved PCEs of 26.39% and 24.89%, respectively. Furthermore, the device showed enhanced stability, retaining 90% of its initial PCE after 1500 hours of operation under 1-sun illumination. Our work presents a feasible route to enhance device stability by optimizing and functionalizing the interfacial layer.

[a] State Key Laboratory of Alternate Electrical Power System with Renewable Energy Sources, North China Electric Power University, Beijing 102206, China. E-mail: hhuang@ncepu.edu.cn, mcli@ncepu.edu.cn

[b] Key Laboratory of Advanced Light Conversion Materials and Biophotonics, School of Chemistry and Life Resources, Renmin University of China, Beijing 100872, China

Introduction

Metal halide perovskite solar cells (PSCs), as transformative technology in the field of photovoltaics, are considered promising candidates for efficient conversion of solar energy, achieving tremendous progress in power conversion efficiency (PCE) with a certified value exceeding 26%.[1] Notably, inverted PSCs have received significant attention owing to their advantages of simple fabrication, great amenability to charge extraction layers, and compatibility in tandem solar cells.[2–7] In the past

three years, the efficiency of inverted PSCs has witnessed rapid progress, mainly resulting from the massive research on hole transport layer (HTL) materials and the buried interface. Among the HTL materials, NiO_x, an inorganic p-type semiconductor, is commonly utilized because of its cost-effectiveness and scalability.[8,9] However, the presence of surface defects, mismatched energy levels with the perovskite, and undesirable interface chemical reactivity hinder the fabrication of high-efficiency inverted PSCs with excellent stability.

The diverse high-oxidative-state Ni species on the surface of NiO_x make the surface chemistry of the NiO_x layer complicated, resulting in perovskite decomposition through diverse chemical reactions between NiO_x and the perovskite at the hetero-interface.[10,11] It has been reported that the detrimental reaction between $Ni^{>3+}$ and the organic cation of the perovskite induces A-site defects at the NiO_x/perovskite interface, and the reaction between $Ni^{>3+}$ and I^- of the perovskite induces l_2 and l_3^-, limiting the efficiency improvement and stability enhancement of NiO_x-based PSCs.[12,13] Considering the undesirable interface chemical reactivity, mismatched energy levels with the perovskite, and interfacial defects, various strategies have been developed to modify the NiO_x/perovskite interface, such as the utilization of organic additives, buffer layers, and inorganic salts.[14–16] Among these strategies, the use of self-assembled monolayers (SAMs) has emerged into the spotlight owing to its distinct advantage of promoting interfacial carrier transport. At present, phosphonic acid SAMs with a carbazole core are the star materials, enabling advances in the performance of inverted PSCs by serving as interfacial materials at the NiO_x/perovskite interface.[17,18] For example, [4-(3,6-dimethyl-9H-carbazol-9-yl)butyl]phosphonic acid (Me-4PACz) was utilized to construct a buffer layer at the NiO_x/perovskite interface, which can optimize the energy level between NiO_x and $FAPbI_3$ (FA is formamidine).[17] However, although these SAMs have been employed to modify the NiO_x/perovskite interface, achieving high-density, closely packed SAMs remains challenging, resulting in an inhomogeneous distribution, and accordingly undesirable aggregates.[19–22] Moreover, although the utilization of SAMs as the buffer layer at the NiO_x/perovskite interface can help mitigate the interfacial reactivity,[23,24] NiO_x still has a potential impact on the perovskite stability, especially considering the inhomogeneous dispersion of SAM materials. Therefore, it is highly desirable to develop strategies to collaboratively optimize the deposition of SAMs and suppress the undesirable interfacial reactions, further leading to high-efficiency inverted PSCs with enhanced stability.

Herein, methylene blue (MB) was co-absorbed with Me-4PACz to fabricate a functionalized interfacial layer, attempting to optimize and stabilize the buried interface. Our research proved that methylene blue could mitigate the uneven dispersion of Me-4PACz on the surface of NiO_x, which reduced the generation of voids and aggregates, providing a flattened and compact buried interface. After co-absorbing methylene blue, the conductivity of the interfacial layer also increased, contributing to the accelerated interfacial carrier transport. Moreover, methylene blue could serve as a redox mediator to selectively reduce the high-valence state of

Ni species and oxidize metallic Pb^0, while synergistically passivating interfacial defects by constructing a bridge-link structure, which effectively enhanced the stability of the buried interface. These advantages translated into an improved efficiency and enhanced stability in inverted PSCs, in which the inverted PSCs with an aperture area of 0.08 cm^2 achieved a PCE of 26.39%, while the inverted PSCs with an aperture area of 1 cm^2 achieved a PCE of 24.89%. Furthermore, the device could retain 91% of its initial PCE after 1500 h of UV irradiation in an N_2-glovebox, and also retained 90% of its initial PCE after 1500 h of operation under 1-sun illumination.

Results and discussion

Modified interfacial layer

It has been reported that the undesirable chemical reaction between NiO_x and the perovskite severely influence the interface stability, which can also be influenced by the inhomogeneous dispersion of SAM and interfacial defects. Considering suitable redox ability that may reduce $Ni^{>3+}$ and oxidize Pb^0, and a molecular configuration that can form π–π interactions with SAM and passivate interfacial defects, MB was chosen to modify the interfacial layers, attempting to enhance the interface stability. We attempted to utilize the MB (molecular structure shown in Fig. S1, ESI†), a redox molecule with a cation possessing variable valences, to modify the SAM (Me-4PACz) interfacial layer at the buried interface in inverted p–i–n PSCs (schematic diagram of the device structure shown in Fig. S2, ESI†), and the anion of Cl^- was reported to have a positive effect on passivating the interface defects.[25–27] In the following discussion, the sample with the Me-4PACz interfacial layer was named normal, while the sample with Me-4PACz & MB as the interfacial layer was named target, where the optimal amounts of MB was preliminarily determined through experimental exploration (Fig. S3 and Supplementary Note S1, ESI†). Before exploring the influence of MB on the properties of the interfacial layer, X-ray photoelectron spectroscopy (XPS) characterization was performed to confirm the steady co-absorbance of the MB molecule on the surface of NiO_x together with Me-4PACz. This was evidenced by the distinct S 2p signal with a peak area ratio to P 2p of approximately 1 : 3 (Fig. 1a and Fig. S4, ESI†).[28] Subsequently, we sought to explore the changes in the surface energy levels of the SAM layer. Ultraviolet photoelectron spectroscopy (UPS) revealed that the SAM showed a negative shift in its Fermi level from −4.46 eV to −4.67 eV (Fig. 1b) after incorporating MB.[29,30] This negative shift in the Fermi level was also validated by results of Kelvin probe force microscopy (KPFM), in which the surface potential of the target layer was higher than that of the control layer (Fig. 1c).[31] The corresponding atomic force microscopy (AFM) images are shown in Fig. S5 (ESI†). The decreased Fermi level induced by MB is supposed to promote interfacial hole transport. In addition, conductive atomic force microscopy (C-AFM) was employed to assess the conductivity of SAM. As shown in Fig. 1d, the average surface current of the target layer was 6.81 nA, which is
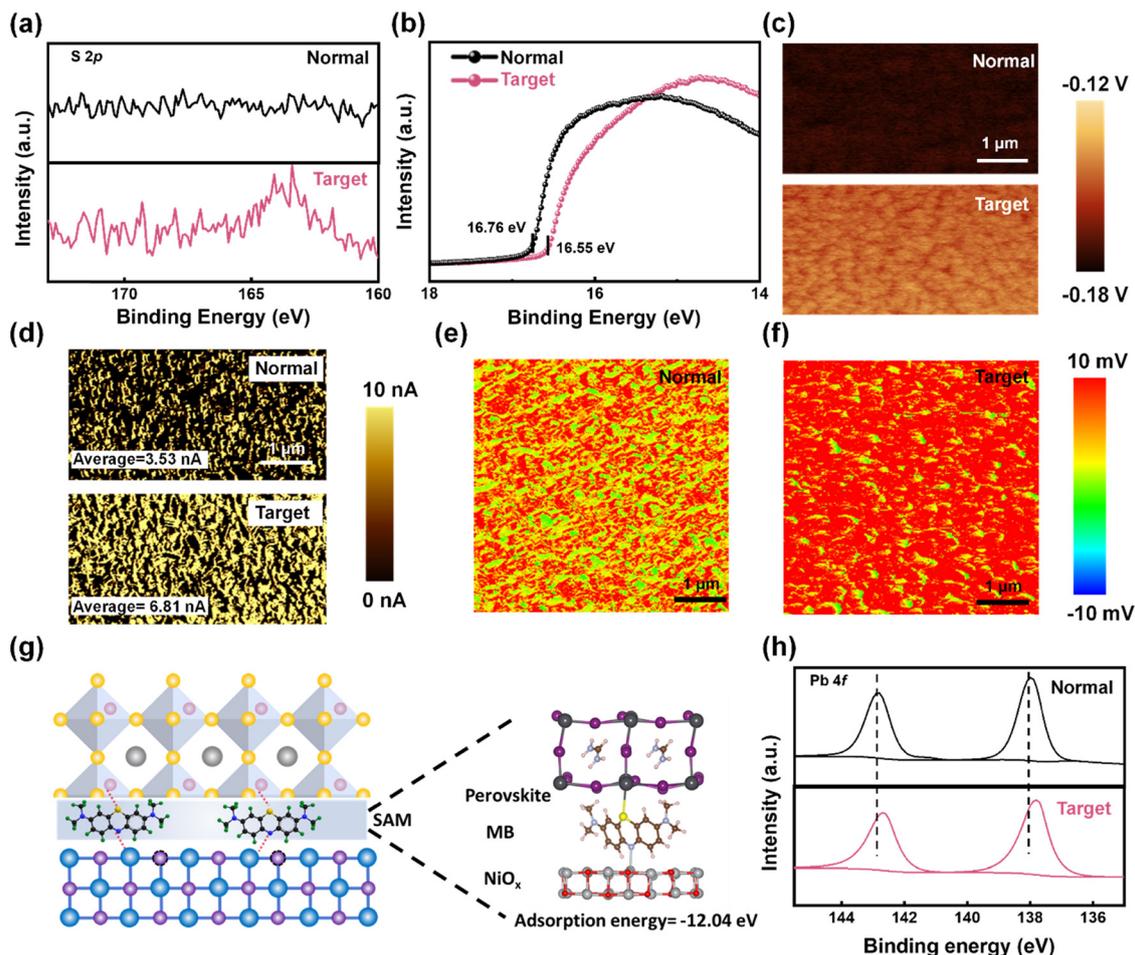
Fig. 1 Modification and functionalization of MB in SAMs. (a) S 2p spectra of the normal and target SAM. (b) UPS spectra of the normal and target SAM. (c) KPFM image of the normal and target SAM. (d) C-AFM image of the normal and target SAM. (e) and (f) Nano-FTIR images of the normal and target SAM. (g) DFT calculation of MB in the interface. (h) Pb 4f spectra of the normal and target perovskite film (buried interface).

significantly higher than that of 3.53 nA for the normal layer, indicating an improvement in surface conductivity.[32] To characterize the surface distribution of SAM on NiO_x, we employed the advanced nano-FTIR (Fourier transform infrared) technique, with its schematic structure and mechanism depicted in Fig. S6 (ESI†). The extracted data focused on tracking the characteristic stretching vibration of the P=O bond at 1176 cm^{-1}.[33,34] In Fig. 1e and f, the colors represent the magnitude of the photo-induced surface potential. The normal SAM exhibits a red-green alternating pattern, indicating a non-uniform distribution of SAM with discrete regions. In contrast, the target SAM predominantly displays a red color, indicating its more homogeneous dispersion and optimized coverage on the NiO_x surface.[35] The improved homogeneity of SAM dispersed on NiO_x can be attributed to the formed π–π interactions between SAM and MB, which weakened the intermolecular forces among the SAM molecules and increased the dipole moment of the SAM molecule, further helping distribute the SAM and suppressing its aggregation (Fig. S7–S10, ESI†).[36,37]

We hypothesize that the interfacial modification by MB molecules also contributed to interface passivation, considering that the MB molecule possess two electronegative atoms, as validated by the calculated surface electrostatic potential (Fig. S11, ESI†). These electronegative atoms of N and S possess long-pair electrons, which can potentially interact with the metal atoms in NiO_x and the perovskite, respectively. DFT calculation was employed to reveal the interfacial interaction between MB and NiO_x and MB and the perovskite, respectively. The optimized structure model showed that the electronegative N atom in MB preferentially attaches to NiO_x, and the S atoms in MB act as passivating agents to interact with the Pb atom at the buried interface. The calculated adsorption energy for MB at the interface between NiO_x and the perovskite is −12.04 eV, indicating the strong interaction of MB at the buried interface (Fig. 1g). To experimentally explore the interaction between MB and NiO_x, Fourier-transform infrared (FTIR) spectroscopy was performed, which revealed a shift in the peak corresponding to the –C=N– group in MB from 1695 cm^{-1} to 1686 cm^{-1} after it was spin-coated on the surface of NiO_x (Fig. S12, ESI†). Additionally, to experimentally characterize the interactions between MB and the perovskite, we used a previously reported method (Fig. S13, ESI†) to expose the bottom surface of the perovskite film with a UV-curable adhesive, followed

by XPS characterization.[38] As shown in Fig. 1h, compared to the normal film, the Pb 4f peaks in the target film shifted to lower binding energies, indicating a decrease in the oxidation state of Pb^{2+}, which is related to the formation of a complex between S and the under-coordinated $[PbI_6]^{4-}$. A similar shift was also observed in the I 3d peaks, validating the interaction between MB with the perovskite at buried interface (Fig. S14, ESI†). This interaction between MB and the perovskite is expected to passivate the perovskite defects, which can be partially validated by the slight improvement in the efficiency of the PSCs with the direct incorporation of MB into the perovskite precursor (Fig. S15, ESI†). These results suggest that MB can act as a passivator at the buried interface, which is beneficial for reducing the interfacial carrier loss and enhancing the interface stability.[39–41]

Optimized perovskite crystallization and promoted interface hole transport

The co-absorbed MB molecules effectively modified the dispersion of SAM on the surface of NiO_x, yielding a flat and compact interfacial layer, which is expected to positively influence the perovskite crystallization. Firstly, scanning electron microscopy (SEM) was employed to evaluate the surface morphology of the perovskite films on different substrates. As depicted in Fig. 2a and b, compared to the perovskite film deposited on the normal SAM, the perovskite film deposited on the target SAM exhibited significantly optimized morphological characteristics, manifested as a denser, smoother surface with a slight increase in grain size.[42,43] Additionally, the AFM images (Fig. S16, ESI†) further confirm this result. Also, we characterized the bottom surface of the perovskite films by peeling them off using a UV-curable adhesive method, which we previously employed when analyzing the bottom surface using XPS. As illustrated in Fig. 2d, the bottom surface of the perovskite film deposited on target SAM exhibited a smooth, void-free morphology, whereas the perovskite films deposited on the normal SAM (Fig. 2c) displayed numerous voids on their bottom surface. X-ray diffraction (XRD) was further conducted to characterize the crystallinity of the perovskite films, and the results are shown in Fig. 2e. Both films exhibited a (100)/(200) preferred orientation, with the corresponding peak positions
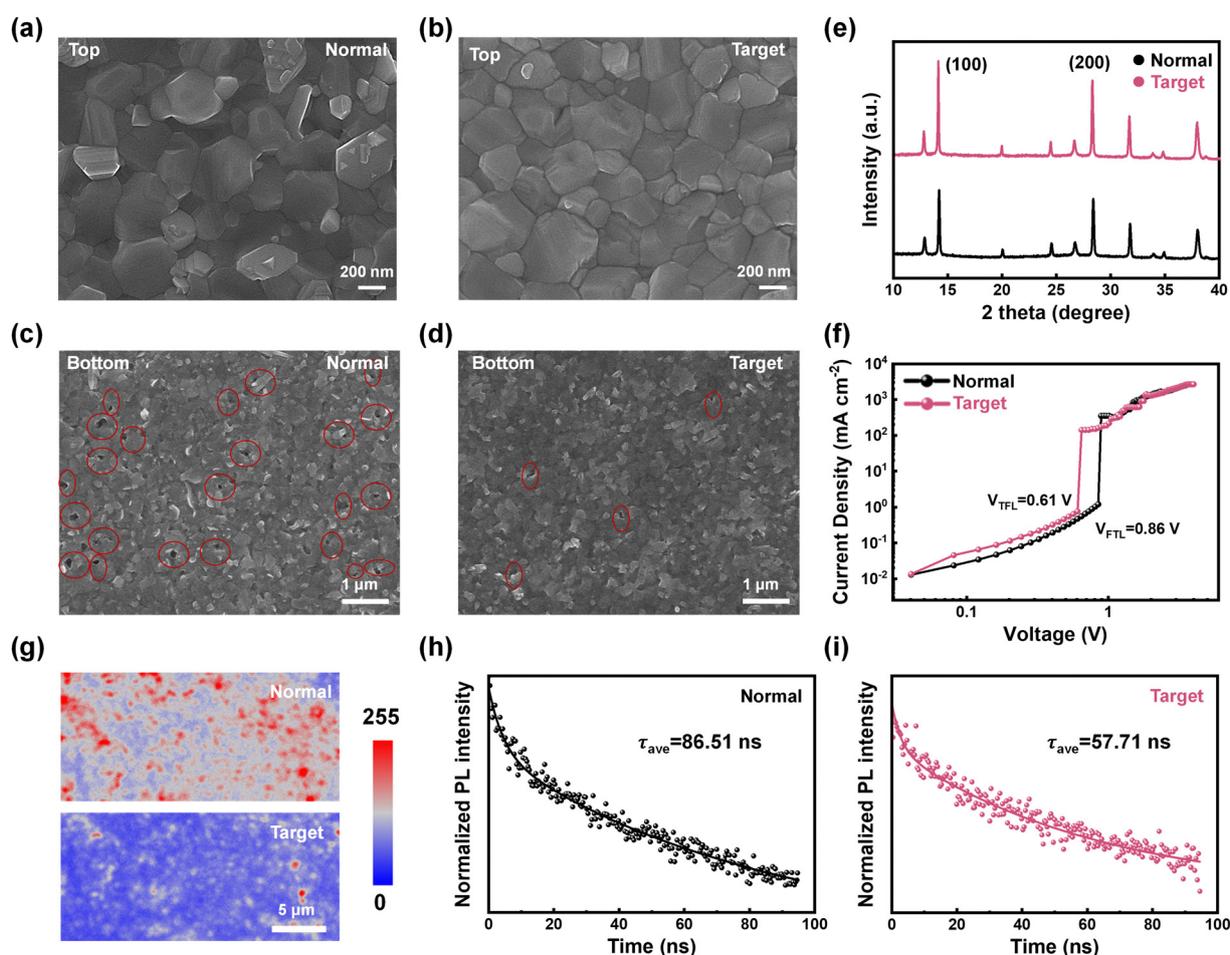

Fig. 2 Improvement in perovskite film deposition and interfacial transport properties. (a) and (b) SEM images of the perovskite film on the normal and target SAM (top). (c) and (d) SEM images of the perovskite film on the normal and target SAM(Bottom). (e) XRD spectra of the normal and target perovskite film. (f) Dark *J*−*V* curves of hole-only devices with various SAMs. (g) PL mapping images of the normal and target perovskite film. (h) and (i) TRPL spectra of perovskite film on the normal and target SAM.

located at 2θ values of approximately $14°$ and $28°$, respectively.[44] In detail, the perovskite film deposited on the target SAM displayed superior crystallinity, which was also validated by the results of grazing-Incidence wide angle X-ray scattering (GIWAXs) (Fig. S17, ESI†). The optimized perovskite crystallization is beneficial for achieving high-quality perovskite films with reduced defects. We fabricated hole-only devices to estimate the defect density in the perovskite films using space-charge-limited current (SCLC) measurements (Fig. 2f). The trap-filled limit voltage (V_{TFL}) is a critical parameter for evaluating the defect density in materials.[45] The defect density (N_{trap}) in the films was calculated according to the formula $N_{trap} = 2\varepsilon_r\varepsilon_0 V_{TFL}/eL^2$, where ε_r is the relative permittivity, ε_0 is the vacuum permittivity, e is the electronic charge, and L is the thickness of the perovskite film (Fig. S18, ESI†). The V_{TFL} of the target device is 0.61 V, giving an N_{trap} of 9.10×10^{15} cm^{-3}, while the V_{TFL} of the normal device is 0.86 V, giving an N_{trap} of 1.28×10^{16} cm^{-3}. The reduced defect density of perovskite film may result from the passivated interfacial defects and optimized perovskite crystallization.

After characterizing the perovskite films on different SAM substrates, we also explored the interfacial carrier transport dynamics using the photoluminescence (PL) mapping and time-resolved photoluminescence (TRPL) techniques.[46,47] Firstly, the PL mapping results (Fig. 2g) demonstrate that the PL intensity of the perovskite films on the target SAM is significantly lower compared to that on the normal SAM, suggesting more efficient hole extraction. The TRPL data, as shown in Fig. 2h and i, revealed that the perovskite film on the target SAM layers exhibits a smaller average lifetime (τ_{avg}) of 57.71 ns compared to 86.51 ns for the perovskite film on normal SAM layers. The τ_{avg} was calculated using the formula $\tau_{avg} = (A_1 \times \tau_1^2 + A_2 \times \tau_2^2)/(A_1 \times \tau_1 + A_2 \times \tau_2)$, where A_1 and A_2 are the amplitudes and τ_1 and τ_2 are the lifetimes obtained from biexponential fitting. The reduced average carrier lifetime also indicates the promoted interfacial hole extraction. To further explore efficacy of MB in inverted PSCs, the TPV (transient photovoltage) and TPC (transient photocurrent) techniques were employed to measure the charge transport and recombination lifetime, respectively.[48] As shown in Fig. S19 (ESI†), the photovoltage decay time increased from 8.89 μs in the control PSCs to 26.24 μs in the target PSCs, indicating a longer charge recombination lifetime. This extended carrier lifetime in the target PSCs suggests the suppression of defect-assisted charge recombination. The TPC decay curves revealed a shorter charge extraction time of 0.89 μs in the target device, indicating faster-photogenerated carrier extraction, which is consistent with the TRPL results. Overall, the TPC and TPV measurements confirmed that the SAM incorporating MB can effectively promote the interfacial charge carrier extraction, reducing hole accumulation and recombination losses at the buried interface.

Suppressed interfacial redox reactions

Here, we discuss the suppressed detrimental interfacial reaction. The variety of Ni species has been reported to induce the redox reaction with the perovskite, decomposing the perovskite at the NiO$_x$/perovskite interface. In detail, the under-coordinated metal cation sites (Ni$^{>3+}$) act as both a Lewis acid and oxidant,

resulting in the deprotonation of cation and I$^-$ oxidation (Fig. 3a). The MB molecule contains multiple nitrogen atoms and aromatic rings, which can accept electrons and provide electrons to other materials, making it redox active. MB also possesses a variety of valances, presenting +1 and +2. We speculate that MB can serve as an interfacial redox mediator, meaning that it can selectively reduce high-valence-states Ni species (Ni$^{>3+}$), and also oxidize metallic Pb^0, preventing the harmful interface reaction and stabilizing the interface (Fig. 3a). To explore the redox reaction between the high-valence states of Ni species (Ni$^{>3+}$) and MB molecules, we carried out XPS measurements to characterize the valence states of Ni species covered by SAM or SAM with MB. The Ni 2p$_{3/2}$ spectra were deconvoluted referring to a previous article.[12] As shown in Fig. 3b, the peaks located at 854.35, 856.12, and 858.75 eV correspond to Ni^{2+}, Ni^{3+}, and Ni^{4+}, respectively. After incorporating MB into the SAM, the captured Ni^{4+} species was obviously reduced, indicating the redox reaction between Ni^{4+} and MB. The reduced Ni^{4+} species in the control film can also be validated by the changes in the absorption spectra, as shown in Fig. 3c. To amplify this redox reaction, we performed UV-ozone (UVO) surface treatment, a method used to oxidize the low-valence-state Ni species, and then increase the Ni^{4+} species, to make the formerly transparent NiO$_x$ film a semitransparent film with a light black color (Fig. S20, ESI†).[49] After coating SAM with MB, a bleaching effect in the UVO-treated NiO$_x$ film could be observed, confirming the reduction of Ni^{4+} species through the redox reaction with MB. To confirm the oxidation of MB on Pb^0, we firstly performed cyclic voltammetry (CV) measurement to characterize the redox potential of MB. As illustrated in Fig. S21 (ESI†), the redox potential of MB, referenced to the normal hydrogen electrode (NHE), lies between that of Pb (-0.365 V $vs.$ NHE) and I$_2$ (0.536 V $vs.$ NHE), indicating that MB can selectively oxidize Pb^0. Subsequently, we carried out XPS measurements on the perovskite films with and without MB. Before spin-coating, both precursors were aged under UV irradiation for 12 h to amplify the effect of MB on oxidizing Pb^0. As shown in Fig. 3d, in the Pb 4f spectra, there are two additional peaks centered at 141.10 eV and 136.21 eV, which correspond to Pb^0 resulting from the decomposition of PbI$_2$ under UV irradiation. In comparison, Pb^0 could not be detected on the film with MB, indicating that Pb^0 can be eliminated by MB through redox reaction.[50,51] XPS measurements were also performed on the films, PbI$_2$, PbI$_2$ with MB, and PbI$_2$ with Me-4PACZ, respectively, validating that MB, not Me-4PACz can effectively suppress Pb^0 (Fig. S22 and S23, ESI†). In addition, we also observed that the peaks in the Pb 4f spectra show a shift after incorporating MB, which confirms the interaction between the Pb atom and MB molecule, validating the DFT results discussed above in Fig. 1g. These results proved that MB can serve as a redox mediator to suppress the detrimental interfacial reaction by reducing the high-valence-state Ni species (Ni$^{>3+}$) and oxidizing Pb^0, enhancing the interface stability.

Photovoltaic performance of PSCs

We fabricated PSCs with the structure shown in Fig. S2 (ESI†), and then evaluated their photovoltaic performance. Firstly, we
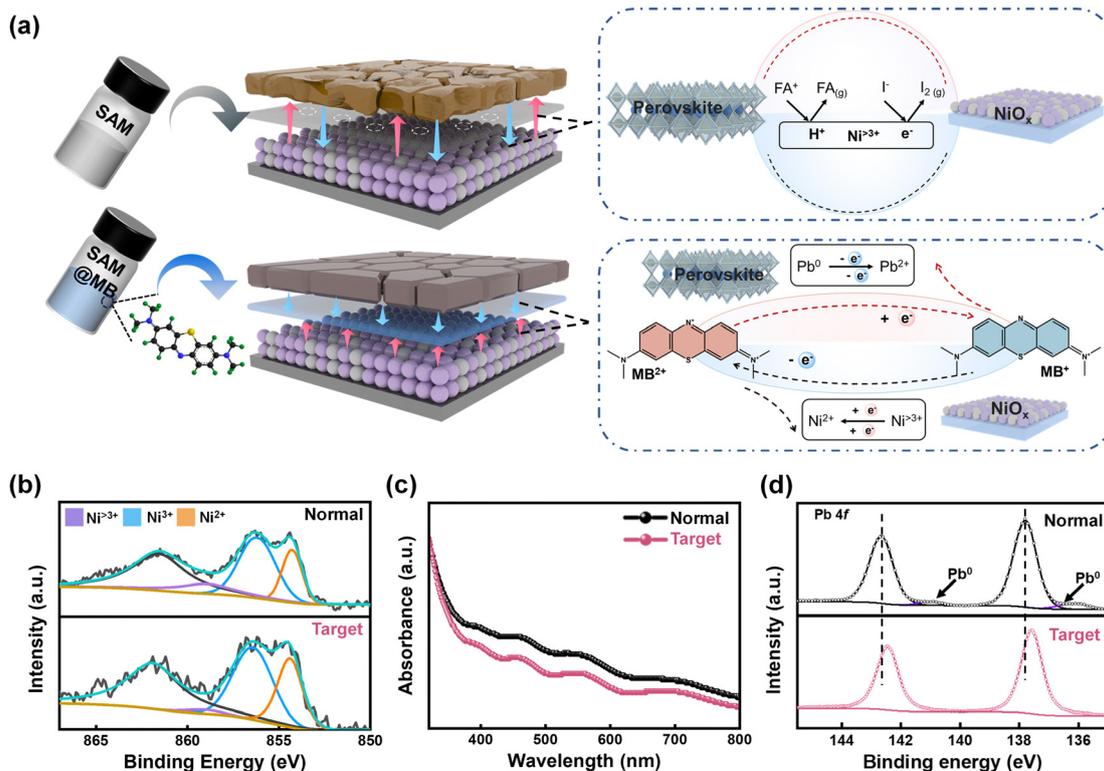
Fig. 3 Inhibition of interfacial redox reactions. (a) Diagram and equations of interfacial redox reactions. (b) Ni 2p spectra of the normal and target SAMs (based on the NiO_x layer). (c) UV-vis absorption spectra of normal and target SAMs (based on the aged NiO_x layer). (d) Pb 4f spectra of the normal and target perovskite films.

performed dark current characterization, as illustrated in Fig. 4a. The dark saturation current density (J_0) was effectively suppressed in the target PSCs, which mainly resulted from the promoted interfacial hole extraction and reduced non-radiative carrier recombination. The increased recombination resistance calculated based on the electrochemical impedance spectroscopy (EIS) data also validated the reduced carrier recombination after interface modification (Fig. S24, ESI†). Besides, the
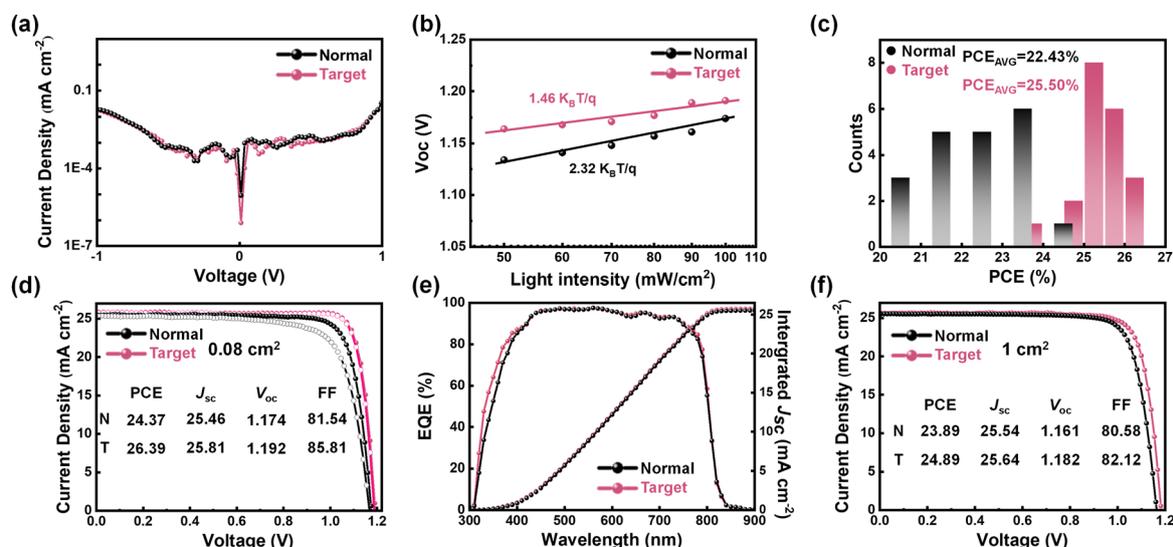

Fig. 4 Photovoltaic performance of normal and target PSCs. (a) Dark J–V curves of SAMs and SAMs with MB-based PSCs. (b) V_{OC} of PSCs with various SAMs plotted against the logarithm of light intensity. (c) Distribution histograms of the PCE values of 20 normal and target PSCs. (d) J–V curves of normal and target PSCs with an active area of 0.08 cm². (e) EQE spectra of the normal and target PSCs. (f) J–V curves of normal and target PSCs with an active area of 1 cm².

relationship between V_{OC} and light intensity was investigated according to the equation $V_{OC} = (n_{ID}k_BT/q) \times \ln(l)$ (where k_B is the Boltzmann constant and q is the elementary charge). The ideality factors (n_{ID}) were determined to be 2.32 and 1.46 for the normal PSCs and target PSCs, respectively (Fig. 4b). The lower n_{ID} indicates reduced trap-assisted recombination within the PSCs, which is consistent with the results from the dark current characterization and EIS test. These results for inverted PSCs confirm that MB can effectively reduce the non-radiative carrier recombination, which is beneficial for improving the efficiency of PSCs.

We prepared 20 target PSCs and 20 normal PSCs, respectively, and then recorded their photovoltaic parameters. As illustrated in Fig. 4c, the PCE distributions for these PSCs reveal that the average PCE of the target PSCs is 25.50%, surpassing that (22.43%) of the normal PSCs. Additionally, statistical analysis of other photovoltaic parameters was also carried out (Fig. S25, ESI†), showing that the improvement in PCE after incorporating MB in the interfacial layer mainly

resulted from the improved V_{OC} and FF. Notably, as seen in Fig. 4d, the target PSCs achieved the maximum PCE of 26.39%, with a short-circuit current density (J_{SC}) of 25.81 mA cm^{-2}, open-circuit voltage (V_{OC}) of 1.192 V, and fill factor (FF) of 85.81%. In contrast, the normal PSCs achieved the maximum PCE of 24.37%, with a J_{SC} of 25.46 mA cm^{-2}, V_{OC} of 1.174 V, and FF of 81.54%. The specific parameters under forward and reverse scans for the champion PSCs are presented in Table S1 (ESI†). The external quantum efficiency (EQE) spectra (Fig. 4e) were also measured, where the integrated J_{SC} values of both the normal and target PSCs show a small variation with that obtained from the J–V measurements.

We also fabricated PSCs with an active area of 1 cm^2. As illustrated in Fig. 4f, the target PSCs achieved the maximum PCE of 24.89%, which is significantly higher than that of the normal PSCs of 23.89%. The specific parameters under forward and reverse scans for these PSCs are presented in Table S2 (ESI†). Additionally, we produced an additional set of 10 target 1 cm^2-PSCs, with their performance parameters presented in
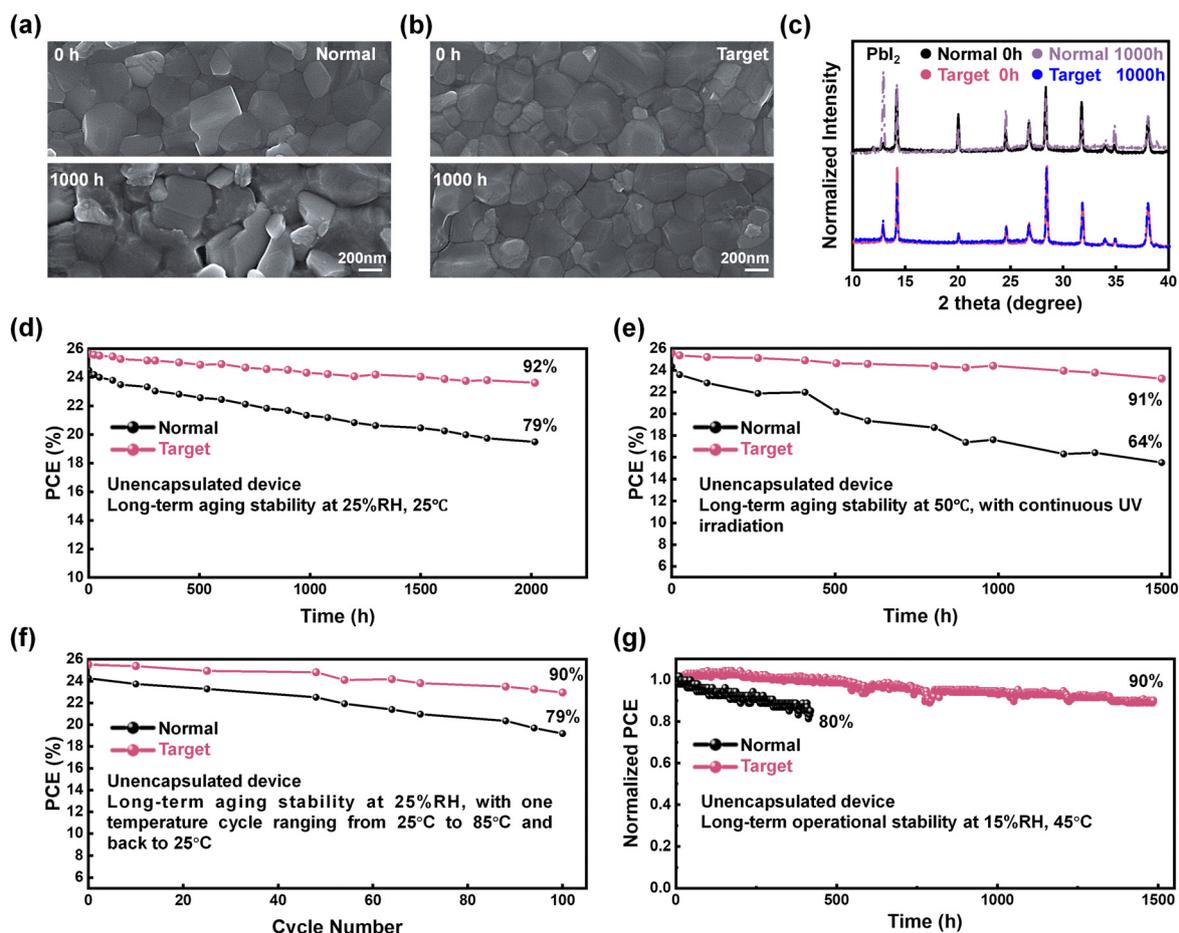

Fig. 5 Accelerated stability tests. (a) and (b) SEM images of the normal and target films. Both films were stored under ambient conditions with an RH of 35% for 1000 h. (c) XRD spectra of the normal and target films. Both films were stored under ambient conditions with an RH of 35% for 1000 h. (d) Long-term stability of unencapsulated devices stored under ambient conditions of 25% RH and 25 °C. (e) Long-term stability of unencapsulated devices stored under continuous UV irradiation with an intensity of 50 mW cm^{-2} in an N$_2$ glove box. (f) Long-term stability of unencapsulated devices at 25% RH, with temperature cycles ranging from 25 °C to 85 °C and back to 25 °C. (g) Operational stability of the unencapsulated devices under continuous simulated AM1.5 illumination at the maximum power point and approximately 15% RH at 45 °C in a glovebox.

Table S3 (ESI†), showing an average PCE of 24.39%. These results elucidate the advantageous role of MB molecules in the functionalization of SAM and interface modification, thereby substantiating the potential and efficacy of MB for fabricating PSCs with a large aperture area.

Enhanced device stability

The MB molecules can effectively reduce the interfacial defects and suppress interfacial redox reactions, thus enhancing the device stability. Accordingly, to systematically evaluate the stability of the perovskite films and the corresponding PSCs, we conducted a series of measurements. Firstly, we assessed the humidity stability of the perovskite films by exposing them to ambient conditions with a relative humidity (RH) of 35% and a temperature of 25 °C for 1000 h. We investigated the film morphology using SEM measurement. As shown in Fig. 5a and b, for the perovskite film deposited on the normal SAM, its decomposition was validated by the visible structural changes observed after storage for 1000 h. In contrast, the perovskite film deposited on the target SAM showed negligible changes in its surface morphology, indicating enhanced stability under the same conditions. We further analyzed the perovskite film in the initial and final stages, respectively, using XRD measurements. In the case of the perovskite film deposited on the normal SAM, the (100) peak intensity significantly decreased, while the intensity of the PbI_2 peak increased after 1000 h of aging (Fig. 5c and Fig. S26, ESI†). This suggests that the perovskite film underwent decomposition under humid conditions. In comparison, the XRD pattern of the perovskite film deposited on the target SAM showed a slight change, indicating that the perovskite film can remain stable after aging in humid air conditions for 1000 h. Following the evaluation of the improved stability of perovskite film, we proceeded to assess the stability of the device. We placed the devices in an environment with approximately 25% RH and 25 °C, and then monitored their efficiency evolution. After aging for 2016 h, the target device retained 92% of its initial PCE, whereas the normal device retained only 79% of its initial PCE (Fig. 5d). Then, harsher conditions were applied to accelerate the aging of the devices for assessing their stability. Firstly, we placed the devices in a nitrogen glovebox at approximately 50 °C under continuous UV irradiation. It was found that the target device retained 91% of its initial PCE after 1500 h, whereas the PCE of the normal device rapidly declined to 64% of its initial value (Fig. 5e). Additionally, we aged the devices under different temperature cycles from 25 °C to 85 °C to 25 °C, in which a cycle lasted for 35 min.[52] The panel parameters during this process are shown in Fig. S27 (ESI†). After 100 cycles, the target device maintained 90% of its initial PCE, while the normal device retained only 79% of its original PCE (Fig. 5f). Finally, we conducted long-term operational stability tests on unencapsulated devices under continuous 1-sun illumination in a glovebox, with controlled conditions of 15% RH and a temperature of 45 °C (Fig. 5g). Remarkably, the target device retained 90% of its initial PCE after 1500 h of operation, while the PCE of the normal device significantly dropped after just 425 h. Based on the above-mentioned stability analysis, it was evident that utilizing the redox MB to functionalize the SAM interfacial layer could enhance the device stability, which is mainly attributed to the stabilized buried interface from the reduced interface defects and suppressed interfacial redox reaction.

Conclusions

In summary, our work demonstrated a redox mediator-functionalized interfacial layer for improving the efficiency and enhancing the stability of inverted PSCs. The in-depth analysis combining both experimental measurements and theoretical calculations revealed that methylene blue could optimize the morphology and electrical properties of Me-4PACz. Moreover, methylene blue could also serve as a redox mediator to selectively reduce the high-valence state of Ni species and oxidize metallic Pb^0, while simultaneously passivating interfacial defects. Owing to the promoted interfacial carrier transport and suppressed interfacial detrimental reaction, the PSCs showed an impressive efficiency of 26.39% with an aperture area of 0.08 cm^2 and 24.89% with an aperture area of 1 cm^2. Furthermore, the device could retain 90% of its initial efficiency after 1500 h of operation under 1-sun illumination and 91% of its initial efficiency after exposure to UV irradiation for 1500 h. Our work presents a valuable reference regarding interface stability enhancement by optimizing and functionalizing the interfacial layer, which provides more opportunities for facile access to commercially available inverted p–i–n PSCs.

Author contributions

M. L., S. Q., and H. H. conceived the idea. M. L. and H. H. guided the work as supervisors. S. Q. and H. H. did experimental designs, device fabrication, and data analysis. F. Y., Y. L., Q. Z., and C. S. were involved in device fabrication and conducted part of the characterizations. S. D. and L. Y. assisted with XRD, XPS spectra, and KPFM testing. P. C. and Z. L. provided support for characterizing the redox reactions. S. Q. and H. H. drafted the initial version of the manuscript. S. D., L. Y., Z. L., X. A., Z. W., and T. J. contributed to the manuscript revision and language polishing. All authors participated in discussing the results and contributed to revising the manuscript.

Data availability

The data supporting this article have been included as part of the ESI.†

Conflicts of interest

There are no conflicts to declare.

Acknowledgements

Notes and references

1 National Renewable Energy Laboratory Best Research-Cell Efficiency Chart (NREL, 2024); **https://www.nrel.gov/pv/cell-eficiency.Html**.

2 Z. Li, B. Li, X. Wu, S. A. Sheppard, S. Zhang, D. Gao, N. J. Long and Z. Zhu, *Science*, 2022, **376**, 416–420.

3 S. Li, Y. Jiang, J. Xu, D. Wang, Z. Ding, T. Zhu, B. Chen, Y. Yang, M. Wei, R. Guo, Y. Hou, Y. Chen, C. Sun, K. Wei, S. M. H. Qaid, H. Lu, H. Tan, D. Di, J. Chen, M. Grätzel, E. H. Sargent and M. Yuan, *Nature*, 2024, **635**, 82–88.

4 Q. Tan, Z. Li, G. Luo, X. Zhang, B. Che, G. Chen, H. Gao, D. He, G. Ma, J. Wang, J. Xiu, H. Yi, T. Chen and Z. He, *Nature*, 2023, **620**, 545–551.

5 S. Li, Y. Xiao, R. Su, W. Xu, D. Luo, P. Huang, L. Dai, P. Chen, P. Caprioglio, K. A. Elmestekawy, M. Dubajic, C. Chosy, J. Hu, I. Habib, A. Dasgupta, D. Guo, Y. Boeije, S. J. Zelewski, Z. Lu, T. Huang, Q. Li, J. Wang, H. Yan, H.-H. Chen, C. Li, B. A. I. Lewis, D. Wang, J. Wu, L. Zhao, B. Han, J. Wang, L. M. Herz, J. R. Durrant, K. S. Novoselov, Z.-H. Lu, Q. Gong, S. D. Stranks, H. J. Snaith and R. Zhu, *Nature*, 2024, **635**, 874–881.

6 H. Chen, C. Liu, J. Xu, A. Maxwell, W. Zhou, Y. Yang, Q. Zhou, A. S. R. Bati, H. Wan, Z. Wang, L. Zeng, J. Wang, P. Serles, Y. Liu, S. Teale, Y. Liu, M. I. Saidaminov, M. Li, N. Rolston, S. Hoogland, T. Filleter, M. G. Kanatzidis, B. Chen, Z. Ning and E. H. Sargent, *Science*, 2024, **384**, 189–193.

7 Y.-H. Lin, Vikram, F. Yang, X.-L. Cao, A. Dasgupta, R. D. J. Oliver, A. M. Ulatowski, M. M. McCarthy, X. Shen, Q. Yuan, M. G. Christoforo, F. S. Y. Yeung, M. B. Johnston, N. K. Noel, L. M. Herz, M. S. Islam and H. J. Snaith, *Science*, 2024, **384**, 767–775.

8 Y. Yang, R. Chen, J. Wu, Z. Dai, C. Luo, Z. Fang, S. Wan, L. Chao, Z. Liu and H. Wang, *Angew. Chem., Int. Ed.*, 2024, **63**, e202409689.

9 S. Liu, J. Li, W. Xiao, R. Chen, Z. Sun, Y. Zhang, X. Lei, S. Hu, M. Kober-Czerny, J. Wang, F. Ren, Q. Zhou, H. Raza, Y. Gao, Y. Ji, S. Li, H. Li, L. Qiu, W. Huang, Y. Zhao, B. Xu, Z. Liu, H. J. Snaith, N.-G. Park and W. Chen, *Nature*, 2024, **632**, 536–542.

10 C. Li, Y. Zhang, X. Zhang, P. Zhang, X. Yang and H. Chen, *Adv. Funct. Mater.*, 2023, **33**, 2214774.

11 Y. Liu, B. Ding, G. Zhang, X. Ma, Y. Wang, X. Zhang, L. Zeng, M. K. Nazeeruddin, G. Yang and B. Chen, *Adv. Sci.*, 2024, **11**, 2309111.

12 C. C. Boyd, R. C. Shallcross, T. Moot, R. Kerner, L. Bertoluzzi, A. Onno, S. Kavadiya, C. Chosy, E. J. Wolf, J. Werner, J. A. Raiford, C. de Paula, A. F. Palmstrom, Z. J. Yu, J. J. Berry, S. F. Bent, Z. C. Holman, J. M. Luther, E. L. Ratcliff, N. R. Armstrong and M. D. McGehee, *Joule*, 2020, **4**, 1759–1775.

13 T. Guo, Z. Fang, Z. Zhang, Z. Deng, R. Zhao, J. Zhang, M. Shang, X. Liu, Z. Hu, Y. Zhu and L. Han, *J. Energy Chem.*, 2022, **69**, 211–220.

14 Y. Jin, H. Feng, Y. Li, H. Zhang, X. Chen, Y. Zhong, Q. Zeng, J. Huang, Y. Weng, J. Yang, C. Tian, J. Zhang, L. Xie and Z. Wei, *Adv. Energy Mater.*, 2024, 2403911.

15 N. Yan, Y. Cao, Z. Jin, Y. Liu, S. Liu, Z. Fang and J. Feng, *Adv. Mater.*, 2024, **36**, 2403682.

16 Q. Cao, T. Wang, X. Pu, X. He, M. Xiao, H. Chen, L. Zhuang, Q. Wei, H. L. Loi, P. Guo, B. Kang, G. Feng, J. Zhuang, G. Feng, X. Li and F. Yan, *Adv. Mater.*, 2024, **36**, 2311970.

17 S. Yu, Z. Xiong, H. Zhou, Q. Zhang, Z. Wang, F. Ma, Z. Qu, Y. Zhao, X. Chu, X. Zhang and J. You, *Science*, 2023, **382**, 1399–1404.

18 Z. Li, X. Sun, X. Zheng, B. Li, D. Gao, S. Zhang, X. Wu, S. Li, J. Gong, J. M. Luther, Z. Li and Z. Zhu, *Science*, 2023, **382**, 284–289.

19 R. Guo, X. Wang, X. Jia, X. Guo, J. Li, Z. Li, K. Sun, X. Jiang, E. Alvianto, Z. Shi, M. Schwartzkopf, P. Müller-Buschbaum and Y. Hou, *Adv. Energy Mater.*, 2023, **13**, 2302280.

20 X. Wang, J. Li, R. Guo, X. Yin, R. Luo, D. Guo, K. Ji, L. Dai, H. Liang, X. Jia, J. Chen, Z. Jia, Z. Shi, S. Liu, Y. Wang, Q. Zhou, T. Wang, G. Pan, P. Müller-Buschbaum, S. D. Stranks and Y. Hou, *Nat. Photonics*, 2024, **18**, 1269–1275.

21 M. Liu, L. Bi, W. Jiang, Z. Zeng, S. W. Tsang, F. R. Lin and A. K. Y. Jen, *Adv. Mater.*, 2023, **35**, 2304415.

22 D. Li, Q. Lian, T. Du, R. Ma, H. Liu, Q. Liang, Y. Han, G. Mi, O. Peng, G. Zhang, W. Peng, B. Xu, X. Lu, K. Liu, J. Yin, Z. Ren, G. Li and C. Cheng, *Nat. Commun.*, 2024, **15**, 7605.

23 Y. Zhou, X. Huang, J. Zhang, L. Zhang, H. Wu, Y. Zhou, Y. Wang, Y. Wang, W. Fu and H. Chen, *Adv. Energy Mater.*, 2024, **14**, 2400616.

24 B. Li, C. Zhang, D. Gao, X. Sun, S. Zhang, Z. Li, J. Gong, S. Li and Z. Zhu, *Adv. Mater.*, 2024, **36**, 2309768.

25 J. Cao, Q. Chen, W. Wu, J. Fu, Z. Zhang, L. Chen, R. Wang, W. Yu, L. Wang, X. Nie, J. Zhang, Y. Zhou, B. Song and Y. Li, *Energy Environ. Sci.*, 2024, **17**, 3454–3469.

26 H. Tan, A. Jain, O. Voznyy, X. Lan, F. P. García de Arquer, J. Z. Fan, R. Quintero-Bermudez, M. Yuan, B. Zhang, Y. Zhao, F. Fan, P. Li, L. N. Quan, Y. Zhao, Z.-H. Lu, Z. Yang, S. Hoogland and E. H. Sargent, *Science*, 2017, **355**, 722–726.

27 H. Min, D. Y. Lee, J. Kim, G. Kim, K. S. Lee, J. Kim, M. J. Paik, Y. K. Kim, K. S. Kim, M. G. Kim, T. J. Shin and S. I. Seok, *Nature*, 2021, **598**, 444–450.

28 S. M. Park, M. Wei, N. Lempesis, W. Yu, T. Hossain, L. Agosta, V. Carnevali, H. R. Atapattu, P. Serles, F. T. Eickemeyer, H. Shin, M. Vafaie, D. Choi, K. Darabi, E. D. Jung, Y. Yang, D. B. Kim, S. M. Zakeeruddin, B. Chen, A. Amassian, T. Filleter, M. G. Kanatzidis, K. R. Graham, L. Xiao, U. Rothlisberger, M. Grätzel and E. H. Sargent, *Nature*, 2023, **624**, 289–294.

29 X. Chu, Q. Ye, Z. Wang, C. Zhang, F. Ma, Z. Qu, Y. Zhao, Z. Yin, H. X. Deng, X. Zhang and J. You, *Nat. Energy*, 2023, **8**, 372–380.

30 S. Tan, T. Huang, I. Yavuz, R. Wang, T. W. Yoon, M. Xu, Q. Xing, K. Park, D.-K. Lee, C.-H. Chen, R. Zheng, T. Yoon, Y. Zhao, H.-C. Wang, D. Meng, J. Xue, Y. J. Song, X. Pan, N.-G. Park, J.-W. Lee and Y. Yang, *Nature*, 2022, **605**, 268–273.

31 Z. Lan, H. Huang, Y. Lu, S. Qu, M. Wang, S. Du, Y. Yang, C. Sun, Q. Zhang, Y. Suo, X. Wang, L. Yan, P. Cui, Z. Zhao and M. Li, *Adv. Funct. Mater.*, 2024, **34**, 2316591.

32 C. Li, L. Chen, F. Jiang, Z. Song, X. Wang, A. Balvanz, E. Ugur, Y. Liu, C. Liu, A. Maxwell, H. Chen, Y. Liu, Z. Wang, P. Xia, Y. Li, S. Fu, N. Sun, C. R. Grice, X. Wu, Z. Fink, Q. Hu, L. Zeng, E. Jung, J. Wang, S. M. Park, D. Luo, C. Chen, J. Shen, Y. Han, C. A. R. Perini, J.-P. Correa-Baena, Z.-H. Lu, T. P. Russell, S. De Wolf, M. G. Kanatzidis, D. S. Ginger, B. Chen, Y. Yan and E. H. Sargent, *Nat. Energy*, 2024, 1–9, DOI: [10.1038/s41560-024-01613-8](https://doi.org/10.1038/s41560-024-01613-8).

33 R. He, W. Wang, Z. Yi, F. Lang, C. Chen, J. Luo, J. Zhu, J. Thiesbrummel, S. Shah, K. Wei, Y. Luo, C. Wang, H. Lai, H. Huang, J. Zhou, B. Zou, X. Yin, S. Ren, X. Hao, L. Wu, J. Zhang, J. Zhang, M. Stolterfoht, F. Fu, W. Tang and D. Zhao, *Nature*, 2023, **618**, 80–86.

34 Y. Zhao, X. Luan, L. Han and Y. Wang, *Adv. Funct. Mater.*, 2024, 2405646, DOI: [10.1002/adfm.202405646](https://doi.org/10.1002/adfm.202405646).

35 C. Fei, A. Kuvayskaya, X. Shi, M. Wang, Z. Shi, H. Jiao, T. J. Silverman, M. Owen-Bellini, Y. Dong, Y. Xian, R. Scheidt, X. Wang, G. Yang, H. Gu, N. Li, C. J. Dolan, Z. J. D. Deng, D. N. Cakan, D. P. Fenning, Y. Yan, M. C. Beard, L. T. Schelhas, A. Sellinger and J. Huang, *Science*, 2024, **384**, 1126–1134.

36 G. Qu, S. Cai, Y. Qiao, D. Wang, S. Gong, D. Khan, Y. Wang, K. Jiang, Q. Chen, L. Zhang, Y. G. Wang, X. Chen, A. K.-Y. Jen and Z. X. Xu, *Joule*, 2024, **8**, 2123–2134.

37 A. R. Pininti, A. S. Subbiah, C. Deger, I. Yavuz, A. Prasetio, P. Dally, V. Hnapovskyi, A. A. Said, L. V. T. Merino, S. Mannar, S. Zhumagali, B. Vishal, M. Marengo, A. Razzaq, M. Babics, T. G. Allen, E. Aydin, R. Azmi and S. D. Wolf, *Adv. Energy Mater.*, 2024, 2403530, DOI: [10.1002/aenm.202403530](https://doi.org/10.1002/aenm.202403530).

38 X. Zhao, Y. Qiu, M. Wang, D. Wu, X. Yue, H. Yan, B. Fan, S. Du, Y. Yang, Y. Yang, D. Li, P. Cui, H. Huang, Y. Li, N. G. Park and M. Li, *ACS Energy Lett.*, 2024, **9**, 2659–2669.

39 S. Du, H. Huang, Z. Lan, P. Cui, L. Li, M. Wang, S. Qu, L. Yan, C. Sun, Y. Yang, X. Wang and M. Li, *Nat. Commun.*, 2024, **15**, 5223.

40 M. Li, B. Jiao, Y. Peng, J. Zhou, L. Tan, N. Ren, Y. Ye, Y. Liu, Y. Yang, Y. Chen, L. Ding and C. Yi, *Adv. Mater.*, 2024, **36**, 2406532.

41 Z. Huang, Y. Bai, X. Huang, J. Li, Y. Wu, Y. Chen, K. Li, X. Niu, N. Li, G. Liu, Y. Zhang, H. Zai, Q. Chen, T. Lei, L. Wang and H. Zhou, *Nature*, 2023, **623**, 531–537.

42 H. Huang, P. Cui, Y. Chen, L. Yan, X. Yue, S. Qu, X. Wang, S. Du, B. Liu, Q. Zhang, Z. Lan, Y. Yang, J. Ji, X. Zhao, Y. Li, X. Wang, X. Ding and M. Li, *Joule*, 2022, **6**, 2186–2202.

43 L. Yan, H. Huang, P. Cui, S. Du, Z. Lan, Y. Yang, S. Qu, X. Wang, Q. Zhang, B. Liu, X. Yue, X. Zhao, Y. Li, H. Li, J. Ji and M. Li, *Nat. Energy*, 2023, **8**, 1158–1167.

44 P. Shi, Y. Ding, B. Ding, Q. Xing, T. Kodalle, C. M. Sutter-Fella, I. Yavuz, C. Yao, W. Fan, J. Xu, Y. Tian, D. Gu, K. Zhao, S. Tan, X. Zhang, L. Yao, P. J. Dyson, J. L. Slack, D. Yang, J. Xue, M. K. Nazeeruddin, Y. Yang and R. Wang, *Nature*, 2023, **620**, 323–327.

45 Y. Yang, Q. Chang, Y. Yang, Y. Jiang, Z. Dai, X. Huang, J. Huo, P. Guo, H. Shen, Z. Liu, R. Chen and H. Wang, *J. Mater. Chem. A*, 2023, **11**, 16871–16877.

46 Y. Zou, W. Yu, H. Guo, Q. Li, X. Li, L. Li, Y. Liu, H. Wang, Z. Tang, S. Yang, Y. Chen, B. Qu, Y. Gao, Z. Chen, S. Wang, D. Zhang, Y. Chen, Q. Chen, S. M. Zakeeruddin, Y. Peng, H. Zhou, Q. Gong, M. Wei, M. Grätzel and L. Xiao, *Science*, 2024, **385**, 161–167.

47 C. Ma, F. T. Eickemeyer, S. H. Lee, D. H. Kang, S. J. Kwon, M. Grätzel and N. G. Park, *Science*, 2023, **379**, 173–178.

48 Y. Li, S. Yuan, S. Miao, J. Wu, H. Y. Wang, Y. Wang, X. C. Ai and J. P. Zhang, *J. Phys. Chem. C*, 2023, **127**, 14679–14686.

49 R. Islam, G. Chen, P. Ramesh, J. Suh, N. Fuchigami, D. Lee, K. A. Littau, K. Weiner, R. T. Collins and K. C. Saraswat, *ACS Appl. Mater. Interfaces*, 2017, **9**, 17201–17207.

50 S. Wu, Y. Yan, J. Yin, K. Jiang, F. Li, Z. Zeng, S. W. Tsang and A. K. Y. Jen, *Nat. Energy*, 2024, **9**, 411–421.

51 X. Huang, L. Bi, Z. Yao, Q. Fu, B. Fan, S. Wu, Z. Su, Q. Feng, J. Wang, Y. Hong, M. Liu, Y. An, M. Chen and A. K. Y. Jen, *Adv. Mater.*, 2024, **36**, 2410564.

52 Q. Zeng, H. Xiao, Q. Ma, R. Huang, Y. Pan, L. Li, X. Liao, S. Liu, W. Zhang and F. Liu, *Adv. Energy Mater.*, 2024, **14**, 2401279.